Time-Gated Imaging on Live Cancer Cells Using Silicon Quantum Dot Nanoparticles with Long-Lived Fluorescence

Chang-Ching Tu,[†,‡] Kamlesh Awasthi,[†] Kuang-Po Chen,[†] Chih-Hsiang Lin,[†] Morihiko Hamada,[†] Nobuhiro Ohta,*[,†] and Yaw-Kuen Li*[,†]

[†]Department of Applied Chemistry, National Chiao Tung University, Hsinchu, Taiwan 300, ROC
[‡]LumiSands Inc., Seattle, Washington 98105, United States

Ⓢ Supporting Information

ABSTRACT: In this work we demonstrate time-gated confocal fluorescence imaging on live cancer cells immunostained by antibody-conjugated silicon quantum dot nanoparticles (SiQD-NPs) and organic dyes, for simultaneous detection of two biological targets and removal of background autofluorescence. With almost all radiative recombinations occurring through oxide-related defect states located on the SiQD surface, the SiQD-NPs have very long photoluminescence lifetimes of about 25 μs, in contrast to the nanosecond-range lifetimes of other commonly used biological fluoro-

phores. This drastic lifetime difference enables a time-gated imaging method here, in which the time-resolved photon distribution of each pixel of a fluorescence image is measured by using a time-correlated single-photon counting technique. Then, by integrating the photon histogram of each pixel over respective time windows, the long-lived component of the fluorescence image comprising only the fluorescence emitted from the SiQD-NPs is separated from all other short-lived signals resulting from the organic dyes and the cell endogenous luminescence. For instance, the membrane and nucleus of a single cancer cell or two types of cancer cells, immunostained with the SiQD-NPs and the organic dyes, respectively, can be clearly distinguished from each other by time-gating, which otherwise cannot be accomplished by conventional multiplexing due to spectral overlap in the wavelength domain.

KEYWORDS: silicon quantum dots, time-gated imaging, immunofluorescence, bioconjugation, biological labels
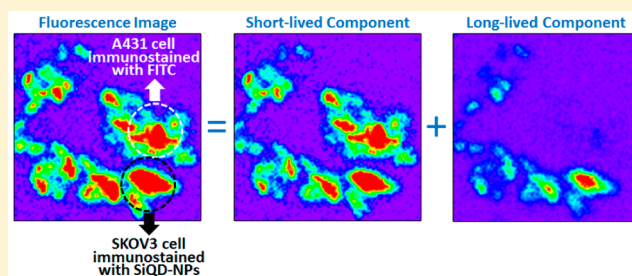
Fluorescent silicon nanomaterials, such as porous silicon nanoparticles and micelle-encapsulated silicon quantum dots,[1−3] owing to their exceptional biocompatibility and biodegradability, have shown great potential as biomedical markers and drug carriers for cancer diagnosis and therapeutics. Particularly, unlike conventional direct band gap semiconductor quantum dots, which emit photoluminescence (PL) predominantly through direct band-to-band transitions, silicon quantum dots (SiQDs) with surface oxidation exhibit a unique PL process: the vast majority of the photoexcited electron–hole pairs are first fast trapped to the oxide-related surface defect states in picoseconds and then recombine slowly in microseconds to emit PL photons.[4−6] Since the transitions occur primarily between two groups of defect states on the edge of the valence and conduction bands, respectively, the oxidized SiQDs have a broad PL bandwidth with a full width at half-maximum (fwhm) of up to 100 nm,[7,8] in contrast to about 30 nm of highly monodisperse CdSe quantum dots, of which the energy band gap is solely determined by the particle size.[9] Furthermore, due to spatial separation of the surface-trapped electron–hole pairs,[4] the oxidized SiQDs have a very long PL lifetime (τ), normally 10 to 30 μs,[10,11] which is at least 2 orders of magnitude longer than the nanosecond-range lifetimes of other commonly used biological fluorophores, such as core–

shell CdSe-ZnS quantum dots (τ = 10.3 ns) and conventional organic dyes (τ = 1 to 5 ns).[12] In addition to the surface-trapping model, the PL lifetime behavior of silicon nanostructures in general can be also explained by the exchange-splitting model, in which the PL radiative lifetime (τ_{rad}) is determined by transitions from the excitonic singlet and triplet states, and the singlet–triplet exchange splitting energy is enhanced due to the spatial confinement of photoexcited excitons.[13,14] Moreover, the high luminescence efficiency of the silicon nanostructures partly results from the exceptionally slow nonradiative process, which is attributed to resonant coupling between the quantum confined electronic states and the surface vibrations of silicon–oxygen bonds, such as Si–O–Si, as revealed by the fine energy splitting of PL spectra observed for the individual porous silicon nanoparticles.[8,14] Lastly, the indirect band gap nature also plays an essential role in the long PL lifetimes of the silicon nanostructures. For instance, the oxygen-free, hydrogen-terminated SiQDs, which emit PL through phonon-assisted quasi-direct band gap recombinations, have low PL radiative
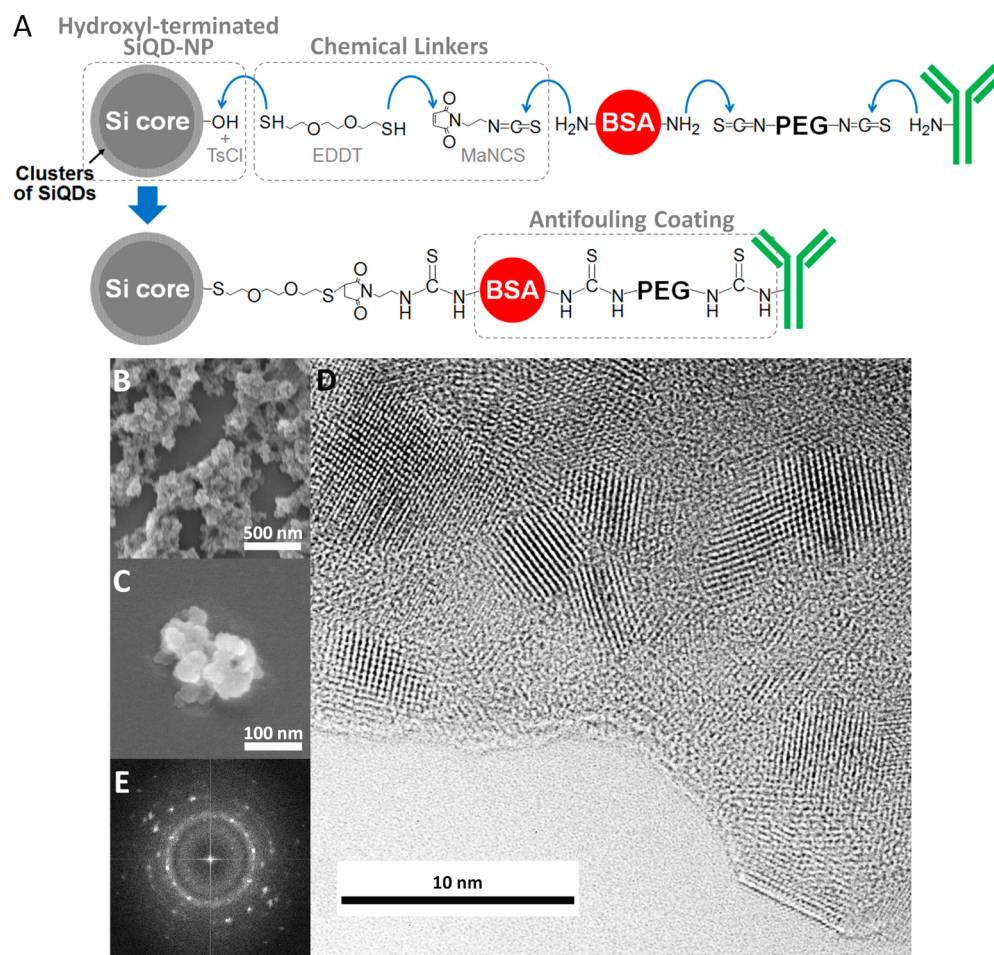
Figure 1. (A) A hydroxyl-terminated SiQD-NP, comprising a Si core and clusters of SiQDs attached on the Si core's surface, is surfaced-activated by *p*-toluenesulfonyl chloride (TsCl), followed by substitution reaction with 2,2′-(ethylenedioxy)diethanethiol (EDDT), to form a thiol-terminated SiQD-NP dispersible in nonpolar organic solvents. For rendering water-solubility and antifouling property, BSA is grafted onto the thiol-terminated SiQD-NP through a short bifunctional linker, 1-(2-isothiocyanatoethyl)-1*H*-pyrrole-2,5-dione (MaNCS), to form a BSA-coated SiQD-NP. Finally, for the immunofluorescence imaging application, the antibody is conjugated to the BSA-coated SiQD-NP through a PEG linker (M_W = 20 000) with both ends functionalized with isothiocyanate (−N=C=S). (B, C) SEM images showing the overall particle size and the specific surface morphology of the thiol-terminated SiQD-NPs. (D) HRTEM image taken at the edge of a thiol-terminated SiQD-NP, showing clusters of sphere-like SiQDs of diameters about 3 to 5 nm attached to a Si core. Direct measurement of the lattice spacing (space group $Fd3m$ and d_{111} = 3.14 Å) confirms the attached SiQDs are composed of crystalline silicon. (E) FFT electron diffraction pattern obtained at the same region as the HRTEM image, confirming that the SiQDs shown in (D), while having different orientations, have high crystallinity.

rates ($k_{rad} = 1/\tau_{rad} = 10^4$ to 10^6 s^{-1}) like the oxidized SiQDs, which, on the contrary, emit PL through surface defect states.[10]

In view of conventional multiplexing, the broad PL bandwidth of the SiQDs can be a major concern, as its spectrum is likely to overlap with the spectra of other fluorophores imaged simultaneously, leading to crosstalk in the wavelength domain between emission filters. On the contrary, in the time domain the long PL lifetime of the SiQDs can be beneficial if a time-gated imaging method is employed, in which pulsed excitation instead of continuous-wave (cw) excitation is used, and the imaging time window following the excitation is properly delayed such that only the slow-decaying fluorescence emitted from the SiQDs is captured. In other words, the fast-decaying fluorescence coming from other labels, such as organic dyes, drops off completely prior to the postponed imaging time window. By identifying which parts of the fluorescence image disappear in the time-gated mode, simultaneous detection of multiple biological targets based on lifetime differences can be achieved. Furthermore, the contrast of the time-gated image is greatly improved, since the

background autofluorescence, which also decays in nano-seconds (τ < 10 ns), is removed by time-gating at the same time.[15] Last but foremost, under conventional cw excitation of high intensity, such as the objective-focused laser beam, the SiQDs with such a long PL lifetime may easily enter into a multiexciton state. Subsequently, inelastic exciton−exciton scattering, Auger recombination, and the blinking effect will likely happen and lower the average photoluminescence quantum yield (PLQY) of the SiQDs.[16] The issue can be alleviated by using the time-gated imaging method. The short time span of the excitation pulse, the relatively low optical power input, and the long intermission after the excitation pulse allow the first photoexcited exciton inside a SiQD to recombine before the second exciton is created. Therefore, the chance of the SiQD entering into the multiexciton state is decreased.

Other biological probes with slow-decaying fluorescence, such as lanthanide probes (τ = 0.6 ms),[17,18] nanoshell-capped or silica-encapsulated transition metal complexes (τ = 10 to 200 ns or 2 μs),[19,20] CdSe quantum dots (τ = 14 ns),[21] and
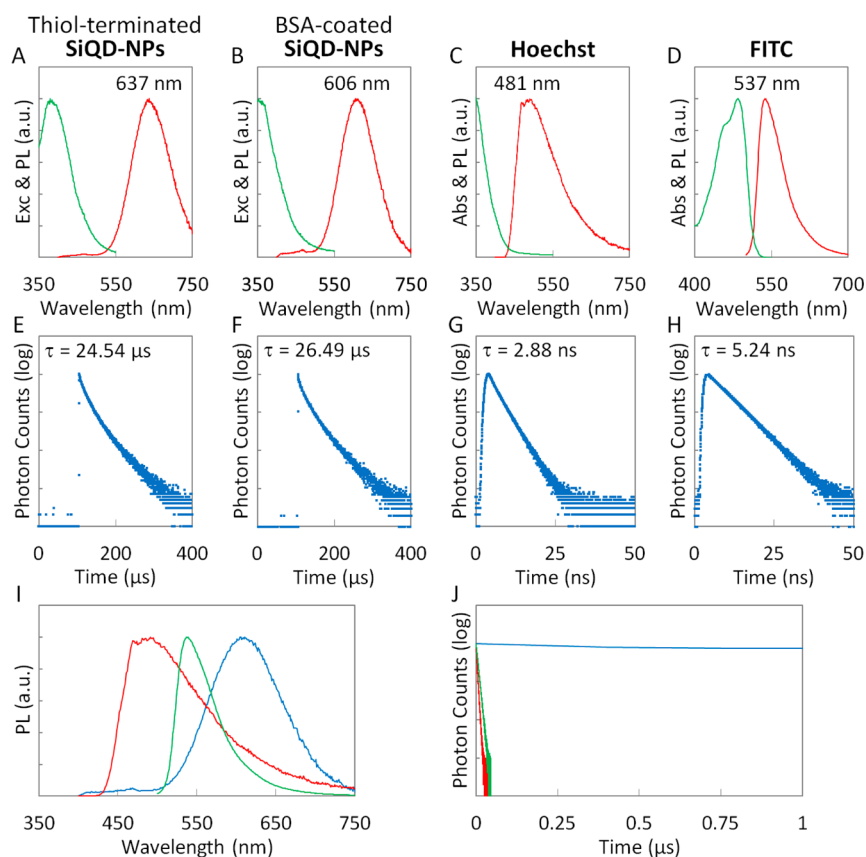
Figure 2. (A, E) Normalized PL (red line, excited by 365 nm) and excitation (green line) spectra and time-resolved PL decay transient (blue dots, excited by 365 nm) of the thiol-terminated SiQD-NPs dispersed in ethyl acetate. (B, F) Normalized PL (red line, excited by 365 nm) and excitation (green line) spectra and time-resolved PL decay transient (blue dots, excited by 365 nm) of the BSA-coated SiQD-NPs dispersed in PB. (C, G) Normalized PL (red line, excited by 350 nm) and absorbance (green line) spectra and time-resolved PL decay transient (blue dots, excited by 365 nm) of Hoechst aqueous solution. (D, H) Normalized PL (red line, excited by 488 nm) and absorbance (green line) spectra and time-resolved PL decay transient (blue dots, excited by 365 nm) of FITC aqueous solution. (I) Normalized PL spectra of the BSA-coated SiQD-NPs (blue line), FITC (green line), and Hoechst (red line) plotted in one graph. (J) Normalized time-resolved PL decay transients of the BSA-coated SiQD-NPs (blue line), FITC (green line), and Hoechst (red line) plotted in one graph (PL, photoluminescence; Exc, excitation; Abs, absorbance).

cadmium-free (Zn)CuInS$_2$ or Zn−Cu−In−Se/ZnS core/shell quantum dots (τ = 21 or 150 ns),[22,23] have been used for time-resolved luminescence imaging. However, these probes are composed of either rare earth metals (e.g., Eu, Tb), transition metals (e.g., Ru), or heavy metals (e.g., Cd, In), all of which are far less biocompatible than silicon,[24,25] especially when under consideration for clinical usage. Recently, time-gated fluorescence imaging of tissues in vivo using biodegradable porous silicon nanoparticles has been realized.[26] With background tissue autofluorescence eliminated by time-gating, more than 100-fold contrast improvement compared to steady-state imaging was achieved.[27] In this work, we further demonstrate in vitro time-gated fluorescence imaging on live cancer cells immunostained by the antibody-conjugated silicon quantum dot nanoparticles (SiQD-NPs) and organic dyes, for the purposes of simultaneous detection of two biological targets and background removal. Additionally, a more versatile time-gated imaging method was developed here: first, the time-resolved photon distribution of each pixel of a fluorescence image is measured by using a time-correlated single-photon counting (TCSPC) technique. Then, the long-lived and short-lived components of the fluorescence image can be obtained by integrating the photon histogram of each pixel over respective time windows. For instance, the membrane and nucleus of a single cancer cell or two types of cancer cells, labeled with the

SiQD-NPs and the organic dyes, respectively, can be clearly separated and detected simultaneously by time-gating.

The brightly fluorescent SiQD-NPs with antifouling coatings composed of bovine serum albumin (BSA) and poly(ethylene glycol) (PEG) are synthesized by a top-down method developed previously.[28] First, a silicon wafer is electrochemically etched in an electrolyte comprising hydrofluoric acid and methanol, creating a red-fluorescing porous silicon layer on the wafer surface, in which microsize Si cores are covered with clusters of nanosize SiQDs. Note that only the SiQDs with diameters less than the exciton Bohr radius of silicon (4.9 nm) are capable of emitting PL. Therefore, the following synthesis steps are mainly for reducing the nonradiative Si cores, at the same time preserving the photoluminescent SiQDs. For this purpose, the porous silicon layer is subsequently treated with 10-undecen-1-ol (UDA) for a photochemical hydrosilylation reaction that passivates the SiQDs with hydrocarbon ligands through silicon carbide bonds. Then, the porous silicon layer is harvested from the wafer surface, and the microsize Si cores are further crumbled into small pieces by high-energy ball milling. The resulting colloid is "selectively" etched in diluted HNO$_3$ and HF, a commonly used etchant for isotropic etching of silicon. During the process, the photoluminescent SiQDs that are passivated with the hydrophobic hydrocarbon ligands in the photochemical hydrosilylation step are protected from the

aqueous etchant and preserved, whereas parts of the non-radiative Si cores not covered with the SiQDs are exposed to the etchant and etched away. Up to this step, the SiQD-NPs of much reduced size are formed, and most remarkably, their outmost surfaces are uniformly terminated hydroxyl groups, some from the hydroxyl ends of UDA bonded on the SiQDs and the other from the silicon oxide capped on the bare silicon surfaces. For rendering the SiQD-NPs' water-solubility and antifouling property, BSA, an exceptionally hydrophilic plasma protein, is grafted onto the hydroxyl-terminated SiQD-NPs through chemical linkers (Figure 1A). Finally, the conjugation to the antibodies is accomplished by a bifunctional polymer, isothiocyanate–PEG–isothiocyanate, of which one end connects to the BSA-coated SiQD-NPs and the other to the antibody both through amine-isothiocyanate coupling (Figure 1A). Notably, all organic capping components discussed here are connected to each other through stable covalent bonding, which is generally considered more stable than micelle encapsulation or physical absorption.

Structural characterizations are performed on the thiol-terminated SiQD-NPs, which can form a clear and stable suspension in a wide range of nonpolar organic solvents, such as ethyl acetate here. Scanning electron microscope (SEM) images of the SiQD-NPs are shown (Figure 1B and C). In overall, the SiQD-NPs have highly porous surfaces and irregular shapes with particle sizes about 100 to 150 nm. The hydrodynamic diameters of the thiol-terminated SiQD-NPs measured by a dynamic light scattering (DLS) method show a similar particle size distribution (Figure S1A). The specific surface morphology of an assembly of the SiQD-NPs observed here (Figure 1B) is in good accordance with other porous silicon nanoparticles of similar sizes.[1] The photoluminescent SiQDs synthesized by the electrochemical etching process, like other porous silicon nanoparticles in the literature,[1,8,11,16,26,27,29] are not freestanding, but rather attached to the nonradiative Si cores whose sizes are significantly reduced from a few micrometers to about 100 to 150 nm by the high-energy ball milling and selective etching steps described earlier. A high-resolution transmission electron microscope (HRTEM) image taken at the edge of a thiol-terminated SiQD-NP is shown (Figure 1D), in which clusters of sphere-like SiQDs of diameters about 3 to 5 nm are found attached to a Si core and their crystalline structures with lattice spacing $d_{111} = 3.14$ Å are clearly visible. The polycrystal-like fast Fourier transform (FFT) electron diffraction pattern (Figure 1E) obtained at the same region as the HRTEM image also confirms the SiQDs in Figure 1D, while having different orientations, have high crystallinity. Lastly, energy-dispersive X-ray analysis (EDXA) is performed on another thiol-terminated SiQD-NP (Figure S2), indicating the nanoparticle is made of pure silicon, with an organic passivating layer involving carbon and oxygen on the particle surface.

Spectral characterizations are performed on the thiol-terminated SiQD-NPs dispersed in ethyl acetate (Figure 2A) and the BSA-coated SiQD-NPs dispersed in 0.1 M pH 6 potassium phosphate buffer (PB) (Figure 2B). With the suspension solvent converted from ethyl acetate to PB, the spectral properties of the SiQD-NPs change accordingly: the PL peak blue-shifted from 637 to 606 nm, the peaks of the excitation spectra also blue-shifted from 379 to 353 nm, and, most dramatically, the PLQY decreased from 42% to 9% (Figure S3A and B, respectively). The change of spectral properties and the enhancement of the nonradiative process

here likely result from Coulomb interaction between the electric dipoles of the physisorbed water molecules and the photoexcited electron–hole pairs trapped at the oxide-related defect states on the SiQD surface of the BSA-coated SiQD-NPs.[29] It is worth mentioning that further conjugation with PEG and antibodies does not change the optical properties of the BSA-coated SiQD-NPs. Although the SiQDs in this work are passivated with hydrocarbon ligands in the photochemical hydrosilylation step, such passivation cannot reach completeness due to steric hindrance of UDA's long alkyl chains.[30] In other words, the SiQD surface is still partially oxidized, especially with Si–O–Si bonds, as evidenced by the strong Fourier transform infrared (FTIR) absorption from 950 to 1250 cm^{-1} (Figure S4).[28] This partial surface oxidation leads to formation of the oxide-related surface defect states, through which almost all radiative recombinations occur. Consequently, with either thiol-termination or BSA-coating, the SiQD-NPs have a broad PL bandwidth (fwhm ≈ 115 nm) and very long PL lifetime (multiexponential decay, $\tau \approx 25$ μs) (Figure 2E and F). Noteworthily, if focusing on the PL dynamics during the first 50 ns after the excitation, fast-decaying components superimposed on the slow-decaying ones become recognizable (Figure S5). The measured PL lifetime ($\tau_{measured}$) is correlated to both the radiative (τ_{rad}) and nonradiative lifetimes (τ_{nonrad}) through the following equation: $1/\tau_{measured} = 1/\tau_{rad} + 1/\tau_{nonrad}$. In a similar manner, the fast-decaying component observed here may result from any radiative or nonradiative processes, which rapidly reduce the population of photoexcited excitons at the lowest quantized states. In the literature, SiQDs synthesized by other methods and also passivated with hydrocarbon ligands through silicon carbide bonds showed similar PL decay transients, i.e., fast-decaying components superimposed on slow-decaying ones.[5] A relaxation model was proposed to explain such PL dynamics: after photoexcitation, an exciton relaxes to the lowest quantized states, from which it can either recombine radiatively or nonradiatively (in nanoseconds) or get trapped to the radiative oxide-related surface defect states and then recombine to emit a PL photon (in microseconds).[5] Particularly, here the fast-decaying component constitutes a larger proportion of the total PL for the BSA-coated SiQD-NPs (Figure S5B) than the thiol-terminated SiQD-NPs (Figure S5A), likely because the slow-decaying PL, which is mediated through the oxide-related surface defect states, is quenched by the physisorbed water molecules, as explained earlier for the dramatic decrease of PLQY. For comparison, the optical properties of two commonly used organic dyes, Hoechst 33342 (Figure 2C and G) and fluorescein isothiocyanate (FITC) (Figure 2D and H), are also characterized. Both dyes exhibit fast-decaying PL (monoexponential decay, $\tau < 10$ ns), which is typical of most organic fluorophores. Meanwhile, Hoechst has a broad PL bandwidth (fwhm = 121 nm), while FITC has a narrow one (fwhm = 55 nm). Considering conventional spectral multiplexing (Figure 2I), the PL spectrum of the SiQD-NPs (blue line) is extensively overlapped with the PL spectra of Hoechst (red line) and FITC (green line), making it impractical to distinguish between respective emissions in the overlapped regions. However, in the time domain (Figure 2J), the very slow-decaying PL emitted from the SiQD-NPs (blue line) can be easily distinguished from other fast-decaying signals (red and green lines) if the imaging time window following the pulsed excitation is delayed for at least 50 ns.

In this work, live cancer cells that are cultured in medium and attached to the bottom of a chamber slide are imaged by an
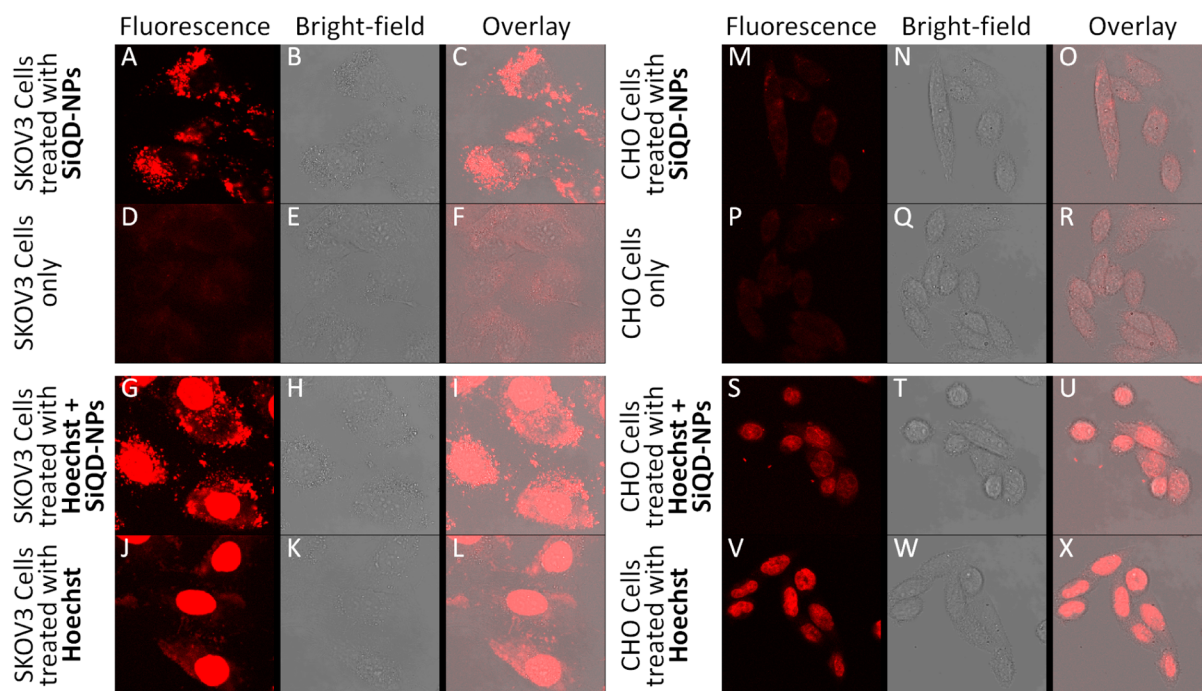
Figure 3. (A−C) SKOV3 cells and (M−O) CHO cells treated with the anti-HER2-conjugated SiQD-NPs. (D−F) SKOV3 cells only and (P−R) CHO cells only. (G−I) SKOV3 cells and (S−U) CHO cells treated with Hoechst and then the anti-HER2-conjugated SiQD-NPs. (J−L) SKOV3 cells and (V−X) CHO cells treated with just Hoechst. For all measurements here, the excitation source is a 405 nm cw laser. The fluorescence images are obtained through a 600-to-700 nm bandpass filter. The physical dimensions of each image here are 98.4 μm × 98.4 μm. The image acquisition settings are the same for all images here.

inverted confocal microscope (TE2000E, Nikon) (Figure S6). A fluorescence image of the cancer cells is constructed by integrating the time-resolved photon distribution, measured by a TCSPC technique, of each pixel of the fluorescence image.[31] The second-harmonic output at 385 or 440 nm generated from a mode-locked Ti:sapphire laser (Tsunami, Spectra-Physics) with pulse duration about 80 fs and repetition rate 5.4 MHz is used as the excitation light. The emission light is passed through a 520 nm long-pass filter and amplified by a microchannel-plate photomultiplier tube (MCP-PMT) before entering into a TCSPC module (SPC-830, Becker & Hickl GmbH). The collected time-resolved data are further analyzed with SPC image software (Becker & Hickl GmbH). Specifically, the short-lived and long-lived components of the fluorescence image are obtained by integrating the measured photon histogram of each pixel over respective time windows.

First we demonstrate that by time-gating the membrane of a single cancer cell immunostained by the SiQD-NPs can be separated from its nucleus stained by Hoechst 33342, a frequently used probe in biomedical imaging to highlight cell nuclei by binding to the deoxyribonucleic acid (DNA) strands. As confirmed by a conventional confocal fluorescence microscope (TSC SP5 II, Leica), the anti-HER2-conjugated SiQD-NPs successfully attach to the membranes of HER2-overexpressing SKOV3 cancer cells (human ovarian carcinoma cells) through antibody−antigen specific binding (Figure 3A−C). In addition, here HER2-nonexpressing CHO cells (Chinese hamster ovarian normal cells) are used as a model to evaluate the degree of nonspecific binding. Due to the effective antifouling coatings composed of BSA and PEG, the non-specific absorption of the anti-HER2-conjugated SiQD-NPs on the CHO cells is negligible (Figure 3M−O). Furthermore, in combination with the SiQD-NPs that are attached on the cell

membrane, Hoechst can stain the cell nucleus to highlight both parts of a SKOV3 cancer cell in parallel (Figure 3G−I). In contrast, only the nuclei of the CHO cells that are also treated with both fluorophores are highlighted (Figure 3S−U). As controls, when treated with Hoechst only, the nuclei of both the SKOV3 cancer cells and the CHO cells become clearly visible (Figure 3J−L and V−X). Lastly, the endogenous cell autofluorescence, compared to the exogenous fluorescence of the SiQD-NPs or Hoechst, is almost indiscernible (Figure 3D−F and P−R).

As pointed out previously, because of the PL spectral overlap (Figure 2I), it is hard to distinguish between fluorescence signals emitted from the SiQD-NPs and Hoechst by using different emission filters, although in this case the nuclei and membranes are seemingly discernible by their shapes and relative positions. To differentiate the two fluorescence signals without any uncertainty, the aforementioned time-gated imaging method is applied to the SKOV3 cancer cells prepared under various conditions. For the SKOV3 cancer cells treated with both the anti-HER2-conjugated SiQD-NPs and Hoechst (Figure 4K−N), both the membranes and nuclei appear in the short-lived component of the fluorescence image. However, only the slow-decaying fluorescence emitted from the SiQD-NPs immunostained on the membranes still exists in the long-lived component. Therefore, by comparing the difference between the short- and long-lived components, the fluorescence signals coming from the SiQD-NPs and Hoechst can be separated and detected simultaneously. As controls, the SKOV3 cancer cells treated with only the anti-HER2-conjugated SiQD-NPs (Figure 4A−D) show the membrane fluorescence signals in both the short- and long-lived components, while the SKOV3 cancer cells treated with only Hoechst (Figure 4P−S) show the nucleus fluorescence signal in the short-lived
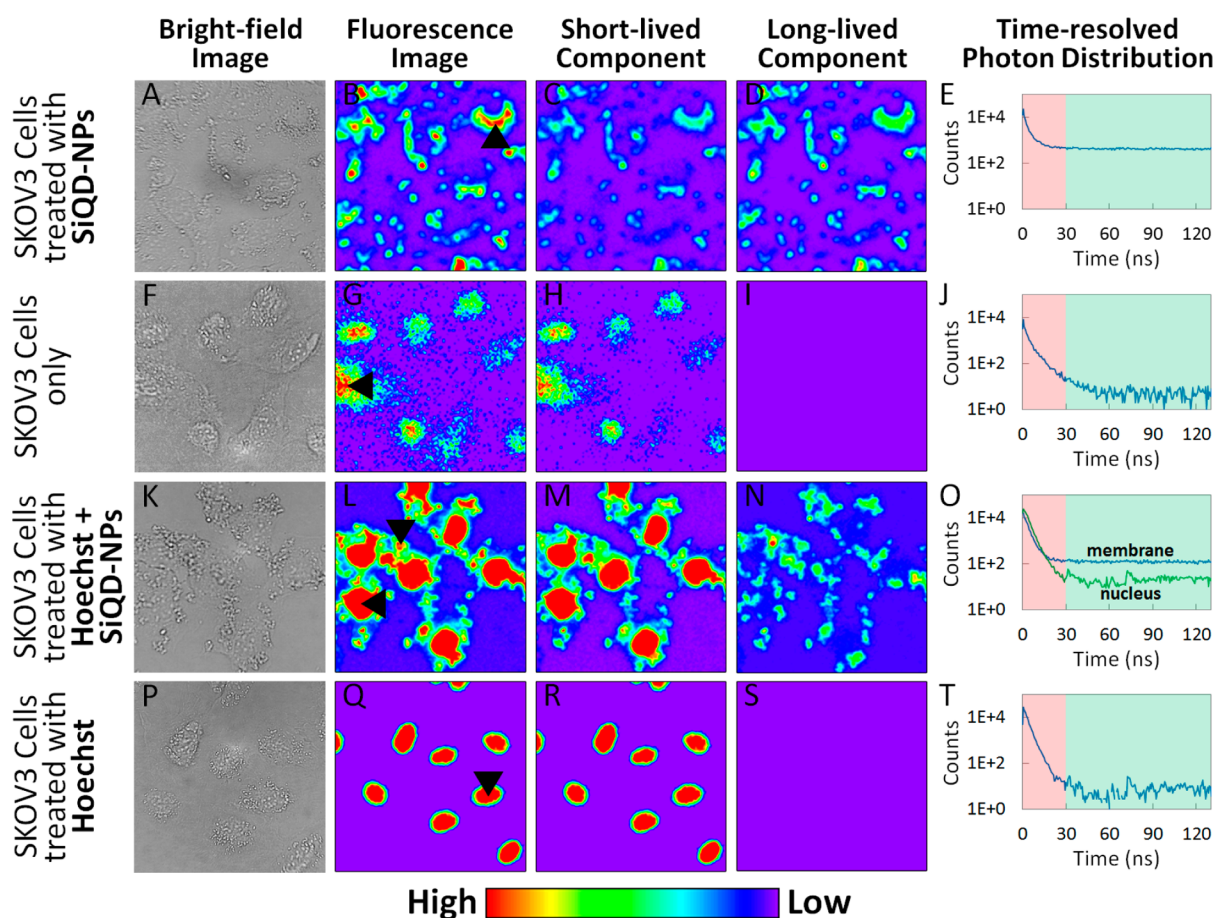
Figure 4. Bright-field images, fluorescence images, short-lived components, and long-live components of the fluorescence images and time-resolved photon distributions of (A−E) SKOV3 cells treated with the anti-HER2-conjugated SiQD-NPs, (F−J) SKOV3 cells only, (K−O) SKOV3 cells treated with Hoechst and then the anti-HER2-conjugated SiQD-NPs, and (P−T) SKOV3 cells treated with just Hoechst, respectively. For all measurements here, the excitation source is a 385 nm pulsed laser with a repetition rate of 5.4 MHz. The fluorescence images are obtained through a 520 nm long-pass filter. The short-lived (C, H, M, R) and long-lived (D, I, N, S) components of the fluorescence images (B, G, L, Q) are formed by integrating the time-resolved photon distribution of each pixel of the fluorescence images over the time windows, 0 to 30 ns (red-shaded area) and 30 to 130 ns (green-shaded area) after the excitation pulse, respectively. The black arrows in the fluorescence images indicate the locations for which the time-resolved photon distributions (E, J, O, T) are shown. The physical dimensions of each image here are 125 μm × 125 μm. It is important to note that the cell autofluorescence of the SKOV3 cells here has much weaker intensity than either the SiQD-NPs or Hoechst, as evidenced by the confocal images in Figure 3. Therefore, the acquisition time for the cells-only image (G) is much longer than other fluorescence images (B, L, Q).

component but nothing in the long-lived one. Most importantly, the time-gated images displaying the SKOV3 membranes here (Figure 4D and N) contain no cell autofluorescence in the background, as the cells-only fluorescence image consists of only the short-lived component (Figure 4F−I).

Besides the cellular images, the time-resolved photon distributions at specific locations of the fluorescence images are also shown. The Hoechst fluorescence at the nuclei (Figure 4T) and the cell autofluorescence (Figure 4J) fast decay mono- and multiexponentially, both with lifetimes about 2.5 ns. Furthermore, the fluorescence of the SiQD-NPs at the membranes (Figure 4E and blue line of Figure 4O) partially decays in nanoseconds at the beginning and then remains almost constant for the rest. The fast-decaying part is attributed to the direct band-to-band radiative or nonradiative recombinations (Figure S5B), rather than the cell autofluorescence, which primarily originates from cell mitochondria,[15] not the cell membranes as specified here. More specifically, based on the excitation (385 nm) and emission window (>520 nm) used here, the cell autofluorescence should belong to nicotinamide

adenine dinucleotide hydrate (NADH) and flavin adenine dinucleotide (FAD) metabolized inside the mitochondria.[32] Interestingly, in Figure 4O, the photon histogram at the nuclei (green line) has a small slow-decaying part, which is about 10 times in photon counts lower than the photon histogram at the membranes (blue line). This is likely due to the antibody− antigen specific binding of the SiQD-NPs to the part of the SKOV3 cell membrane located on top of the nucleus. Although not in the imaging focal plane, which is positioned lower inside the cytoplasm part, their fluorescence can still diffuse downward to the nucleus and therefore contribute to the slow-decaying part here.

Second we demonstrate that by time-gating two types of cancer cells immunostained by the SiQD-NPs and FITC, respectively, can be separated from each other, which otherwise cannot be accomplished by conventional multiplexing in the wavelength domain or simply observing cell morphologies. Under the conventional confocal fluorescence microscope (TSC SP5 II, Leica), the anti-HER2-conjugated SiQD-NPs show significant antibody−antigen specific binding to the HER2-overexpressing SKOV3 cancer cells (Figure 5A−C) and
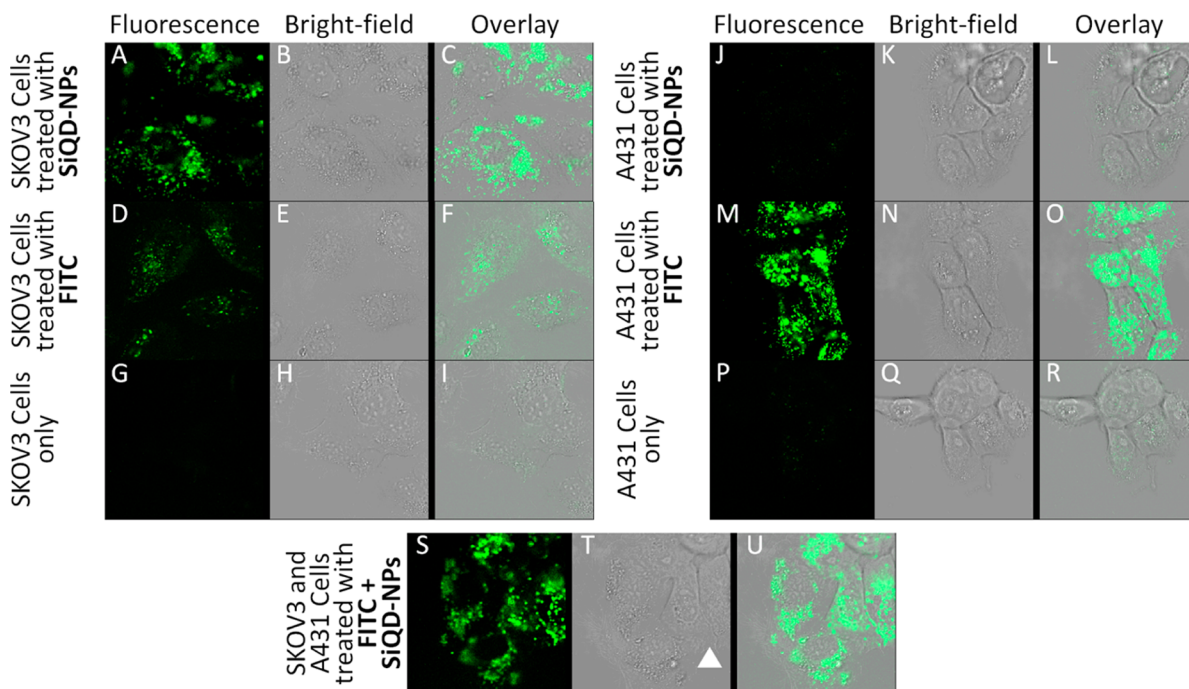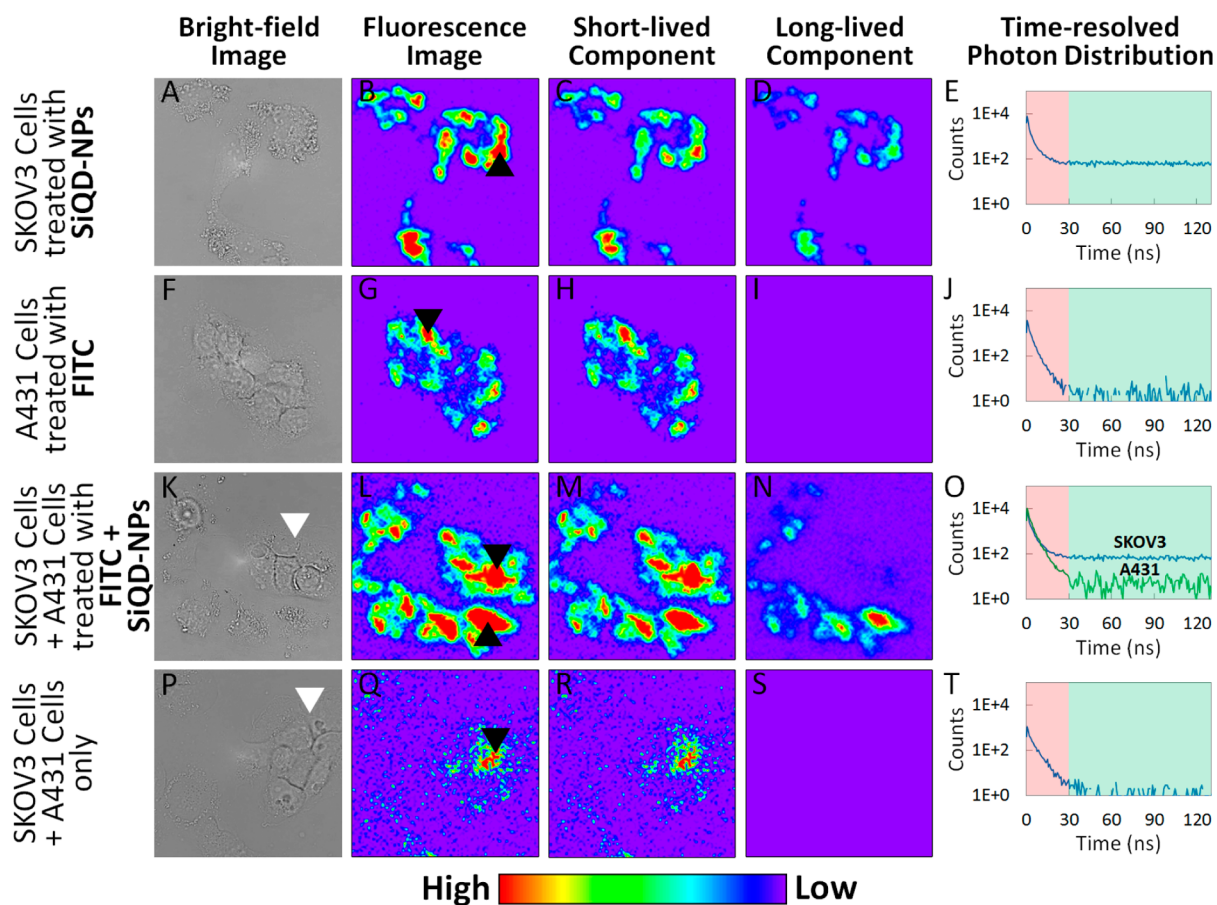
Figure 5. (A−C) SKOV3 cells and (J−L) A431 cells treated with the anti-HER2-conjugated SiQD-NPs. (D−F) SKOV3 cells and (M−O) A431 cells treated with the anti-EGFR primary antibodies, followed by the FITC-conjugated anti-mouse secondary antibodies. (G−I) SKOV3 cells only and (P−R) A431 cells only. (S−U) SKOV3 cells and A431 cells (indicated by a white arrow), which were cultured together side by side, treated with the anti-EGFR primary antibodies, then the FITC-conjugated anti-mouse secondary antibodies, and finally the anti-HER2-conjugated SiQD-NPs. For all measurements here, the excitation source is a 442 nm cw laser. The fluorescence images are obtained through a 500-to-600 nm bandpass filter. The physical dimensions of each image here are 98.4 μm × 98.4 μm. The image acquisition settings are the same for all images here.

negligible binding to A431 cancer cells (human epidermoid carcinoma cells), which overexpress EGFR cell-surface receptors and also have little amount of HER2 (Figure 5J−L).[33] When treated with the anti-EGFR primary antibodies followed by the FITC-conjugated anti-mouse secondary antibodies, the A431 cancer cells shows much stronger immunofluorescence signal (Figure 5M−O), while the SKOV3 cancer cells, which also have little amount of EGFR cell-surface receptors, display slight FITC staining (Figure 5D−F).[33] Most importantly, when both immunostaining procedures are applied to the two types of cancer cells cultured together, the SiQD-NPs and FITC successfully immunostain the SKOV3 and A431 cancer cells, respectively (Figure 5S−U). As controls, relative to the exogenous fluorescence of the SiQD-NPs or FITC, the endogenous autofluorescence of the SKOV3 or A431 cancer cells is minimal (Figure 5G−I and P−R).

Due to the PL spectral overlap between the SiQD-NPs and FITC (Figure 2I), conventional multiplexing in the wavelength domain is essentially infeasible. Moreover, unlike the previous demonstration where the membrane and nucleus of a cancer cell can be easily distinguished from each other by their shapes and positions, the immunostained SKOV3 and A431 cancer cells here look alike in the fluorescence images (Figures 5S and 6L), although in the bright-field images (Figures 5T and 6K,P) the SKOV3 cancer cells are usually much flatter and smoother at the boundaries than the A431 cancer cells. To identify each cell type without ambiguity, the same time-gated imaging method used for the previous demonstration is applied to the SKOV3 and A431 cancer cells immunostained with the anti-HER2-conjugated SiQD-NPs and the FITC-conjugated anti-EGFR antibodies, respectively (Figure 6K−N). Both the SKOV3 and A431 cancer cells appear in the short-lived

component of the fluorescence image, but only the SKOV3 cancer cells immunostained with the SiQD-NPs still exist in the long-lived component. In other words, the cells disappearing in the long-lived component should belong to the A431 cancer cells immunostained with FITC, of which the fast-decaying fluorescence totally diminishes before the time-gating. As controls, the SKOV3 cancer cells treated with only the anti-HER2-conjugated SiQD-NPs show fluorescence signals in both the short- and long-lived components (Figure 6A−D), while the A431 cancer cells treated with only the FITC-conjugated anti-EGFR antibodies show fluorescence signals in the short-lived component but nothing in the long-lived one (Figure 6F−I). The time-resolved photon distributions for FITC immunostained on the A431 cancer cells (Figure 6J and green line of Figure 6O) exhibit monoexponential decay with an average lifetime of about 2.4 ns. On the other hand, the time-resolved photon distributions for the SiQD-NPs immunostained on the SKOV3 cancer cells (Figure 6E and blue line of Figure 6O) remain almost constant, with a fast-decaying part due to the direct band-to-band radiative or nonradiative recombinations (Figure S5B) superimposed on top at the beginning. Lastly, similar to the previous demonstration, the time-gated images of the SKOV3 cancer cells here (Figure 6D and N) are free of background autofluorescence, which fast decays in nanoseconds (Figure 6P−T). Particularly, based on the excitation (440 nm) and emission window (>520 nm) used here, the cell autofluorescence should mostly come from the FAD metabolized inside the cell mitochondria.[32]

In summary, highly fluorescent SiQD-NPs, comprising size-reduced Si cores (about 100 to 150 nm) and clusters of crystalline SiQDs (about 5 nm) attached on the surfaces of the Si cores, are synthesized by a top-down method, including

Figure 6. Bright-field images, fluorescence images, short-lived components, and long-lived components of the fluorescence images and time-resolved photon distributions of (A–E) SKOV3 cells treated with the anti-HER2-conjugated SiQD-NPs, (F–J) A431 cells treated with the anti-EGFR primary antibodies and then the FITC-conjugated anti-mouse secondary antibodies, (K–O) SKOV3 cells and A431 cells (indicated by a white arrow), which were cultured together side by side, treated with the anti-EGFR primary antibodies, then the FITC-conjugated anti-mouse secondary antibodies, and finally the anti-HER2-conjugated SiQD-NPs, and (P–T) SKOV3 cells and A431 cells (indicated by a white arrow) only. For all measurements here, the excitation source is a 440 nm pulsed laser with a repetition rate of 5.4 MHz. The fluorescence images are obtained through a 520 nm long-pass filter. The short-lived (C, H, M, R) and long-lived (D, I, N, S) components of the fluorescence images (B, G, L, Q) are formed by integrating the time-resolved photon distribution of each pixel of the fluorescence images over the time windows, 0 to 30 ns (red-shaded area) and 30 to 130 ns (green-shaded area) after the excitation pulse. The black arrows in the fluorescence images indicate the locations for which the time-resolved photon distributions (E, J, O, T) are shown. The physical dimensions of each image here are 115 μm × 115 μm. It is important to note that the autofluorescence of either the SKOV3 or A431 cells here has much weaker intensity than either the SiQD-NPs or FITC, as evidenced by the confocal images in Figure 5. Therefore, the acquisition time for the cells-only image (Q) is much longer than other fluorescence images (B, G, L).

electrochemical etching, photochemical hydrosilylation, high-energy ball milling, and selective etching. The SiQD-NPs are further coated with BSA and PEG, rendering the nanoparticles' water-solubility, antifouling property and capability of conjugation to the antibodies. Due to steric hindrance of the long alkyl ligands used in the hydrosilylation, the silicon carbide and hydrocarbon passivation on the SiQD surface cannot be thorough. As a result, the SiQD surface is partially oxidized, leading to formation of the oxide-related surface defect states, through which almost all radiative recombinations occur. Consequently, the SiQD-NPs dispersible in water have relatively broad PL bandwidth (fwhm $\approx$ 115 nm) and very long PL lifetime ($\tau \approx$ 25 μs). When used in combination with organic dyes that have nanosecond-range PL lifetimes, the antibody-conjugated SiQD-NPs enable a time-gated immuno-fluorescence imaging method here, for detecting two different biological targets in parallel and removing background autofluorescence. First, the time-resolved photon distribution of each pixel of a fluorescence image is measured by using a TCSPC technique. Then, by integrating the photon histogram

of each pixel over the respective time windows, the long-lived component of the fluorescence image consisting of only the fluorescence emitted from the SiQD-NPs is separated from all other short-lived signals resulting from the organic dyes and the cell autofluorescence. In the first demonstration, the membrane and nucleus of a HER2-overexpressing SKOV3 cancer cell, labeled with the anti-HER2-conjugated SiQD-NPs and Hoechst, respectively, can be separated from each other by time-gating. In the second demonstration, by using the same time-gated imaging method, the SKOV3 cancer cells immunostained with the anti-HER2-conjugated SiQD-NPs can be distinguished from the EGFR-overexpressing A431 cancer cells immunostained with the FITC-conjugated anti-EGFR antibodies. Such demonstrations cannot be accomplished by conventional multiplexing methods due to extensive spectral overlap in the wavelength domain. Most importantly, all the long-lived components of the fluorescence images shown here are free of background autofluorescence, which fast decays in nanoseconds, making the time-gated imaging method here using the antibody-conjugated SiQD-NPs a promising solution

for high-contrast and high-sensitivity immunofluorescence imaging.

ASSOCIATED CONTENT

ⓢ Supporting Information

The Supporting Information is available free of charge on the ACS Publications website at DOI: 10.1021/acsphotonics.7b00188.

> DLS particle size distributions of the SiQD-NPs; EDXA of the SiQD-NPs; spectra for calculating the PLQY of the SiQD-NPs; FTIR-ATR spectra of the SiQD-NPs; time-resolved PL decay transients of the SiQD-NPs within the first 50 ns after the excitation pulse; optical setup for the time-gated imaging method using the SiQD-NPs; experimental section describing the materials used, the synthesis of the anti-HER2-conjugated SiQD-NPs, the characterization, and the immunostaining process in detail (PDF)

AUTHOR INFORMATION

Corresponding Authors

*E-mail (N. Ohta): nohta@nctu.edu.tw. Tel: +886 3 5131395.
*E-mail (Y.-K. Li): ykl@faculty.nctu.edu.tw. Tel: +886 3 5712121, ext. 56545.

ORCID ⓞ

Chang-Ching Tu: 0000-0002-9233-1928

Notes

The authors declare no competing financial interest.

ACKNOWLEDGMENTS

REFERENCES

(1) Park, J.-H.; Gu, L.; Maltzahn, G. v.; Ruoslahti, E.; Bhatia, S. N.; Sailor, M. J. Biodegradable Luminescent Porous Silicon Nanoparticles for In Vivo Applications. *Nat. Mater.* **2009**, *8*, 331–336.

(2) Erogbogbo, F.; Yong, K.-T.; Roy, I.; Hu, R.; Law, W.-C.; Zhao, W.; Ding, H.; Wu, F.; Kumar, R.; Swihart, M. T.; Prasad, P. N. In Vivo Targeted Cancer Imaging, Sentinel Lymph Node Mapping and Multi-Channel Imaging with Biocompatible Silicon Nanocrystals. *ACS Nano* **2011**, *5*, 413–423.

(3) Chinnathambi, S.; Chen, S.; Ganesan, S.; Hanagata, N. Silicon Quantum Dots for Biological Applications. *Adv. Healthcare Mater.* **2014**, *3*, 10–29.

(4) Dohnalová, K.; Kůsová, K.; Pelant, I. Time-Resolved Photoluminescence Spectroscopy of the Initial Oxidation Stage of Small Silicon Nanocrystals. *Appl. Phys. Lett.* **2009**, *94*, 211903.

(5) Sykora, M.; Mangolini, L.; Schaller, R. D.; Kortshagen, U.; Jurbergs, D.; Klimov, V. I. Size-Dependent Intrinsic Radiative Decay Rates of Silicon Nanocrystals at Large Confinement Energies. *Phys. Rev. Lett.* **2008**, *100*, 067401.

(6) Godefroo, S.; Hayne, M.; Jivanescu, M.; Stesmans, A.; Zacharias, M.; Lebedev, O. I.; Tendeloo, G. V.; Moshchalkov, V. V. Classification and Control of the Origin of Photoluminescence from Si Nanocrystals. *Nat. Nanotechnol.* **2008**, *3*, 174–178.

(7) Mastronardi, M. L.; Maier-Flaig, F.; Faulkner, D.; Henderson, E. J.; Kübel, C.; Lemmer, U.; Ozin, G. A. Size-Dependent Absolute Quantum Yields for Size-Separated Colloidally-Stable Silicon Nanocrystals. *Nano Lett.* **2012**, *12*, 337–342.

(8) Mason, M. D.; Credo, G. M.; Weston, K. D.; Buratto, S. K. Luminescence of Individual Porous Si Chromophores. *Phys. Rev. Lett.* **1998**, *80*, 5405–5408.

(9) Jang, E.; Jun, S.; Jang, H.; Lim, J.; Kim, B.; Kim, Y. White-Light-Emitting Diodes with Quantum Dot Color Converters for Display Backlights. *Adv. Mater.* **2010**, *22*, 3076–3080.

(10) Dohnalová, K.; Poddubny, A. N.; Prokofiev, A. A.; Boer, W. D. d.; Umesh, C. P.; Paulusse, J. MJ; Zuilhof, H.; Gregorkiewicz, T. Surface Brightens Up Si Quantum Dots: Direct Bandgap-Like Size-Tunable Emission. *Light: Sci. Appl.* **2013**, *2*, e46.

(11) Kůsová, K.; Cibulka, O.; Dohnalová, K.; Pelant, I.; Valenta, J.; Fučíková, A.; Žídek, K.; Lang, J.; Englich, J.; Matějka, P.; Štěpánek, P.; Bakardjieva, S. Brightly Luminescent Organically Capped Silicon Nanocrystals Fabricated at Room Temperature and Atmospheric Pressure. *ACS Nano* **2010**, *4*, 4495–4504.

(12) Resch-Genger, U.; Grabolle, M.; Cavaliere-Jaricot, S.; Nitschke, R.; Nann, T. Quantum Dots versus Organic Dyes as Fluorescent Labels. *Nat. Methods* **2008**, *5*, 763–775.

(13) Calcott, P. D.; Nash, K. J.; Canham, L. T.; Kane, M. J.; Brumhead, D. Identification of Radiative Transitions in Highly Porous Silicon. *J. Phys.: Condens. Matter* **1993**, *5*, L91–L98.

(14) Saar, A. Photoluminescence from Silicon Nanostructures: the Mutual Role of Quantum Confinement and Surface Chemistry. *J. Nanophotonics* **2009**, *3*, 032501.

(15) Ohta, N.; Nakabayashi, T. Intracellular Autofluorescence Species: Structure, Spectroscopy, and Photophysics. In *Natural Biomarkers for Cellular Metabolism, Biology, Techniques, and Applications*; Ghukasyan, V. V.; Heikal, A. A., Eds.; CRC Press: Boca Raton, 2014; Chapter 2, pp 41–64.

(16) Valenta, J.; Fucikova, A.; Vácha, F.; Adamec, F.; Humpolíčková, J.; Hof, M.; Pelant, I.; Kůsová, K.; Dohnalová, K.; Linnros, J. Light-Emission Performance of Silicon Nanocrystals Deduced from Single Quantum Dot Spectroscopy. *Adv. Funct. Mater.* **2008**, *18*, 2666–2672.

(17) Hanaoka, K.; Kikuchi, K.; Kobayashi, S.; Nagano, T. Time-Resolved Long-Lived Luminescence Imaging Method Employing Luminescent Lanthanide Probes with a New Microscopy System. *J. Am. Chem. Soc.* **2007**, *129*, 13502–13509.

(18) Zhang, L.; Zheng, X.; Deng, W.; Lu, Y.; Lechevallier, S.; Ye, Z.; Goldys, E. M.; Dawes, J. M.; Piper, J. A.; Yuan, J.; Vereist, M.; Jin, D. Practical Implementation, Characterization and Applications of a Multi-Colour Time-Gated Luminescence Microscope. *Sci. Rep.* **2015**, *4*, 6597.

(19) Zhang, J.; Fu, Y.; Lakowicz, J. R. Fluorescent Metal Nanoshells: Lifetime-Tunable Molecular Probes in Fluorescent Cell Imaging. *J. Phys. Chem. C* **2011**, *115*, 7255–7260.

(20) Song, C. H.; Ye, Z. Q.; Wang, G. L.; Jin, D. Y.; Yuan, J. L.; Guan, Y. F.; Piper, J. Preparation and Time-Gated Luminescence Bioimaging Application of Ruthenium Complex Covalently Bound Silica Nanoparticles. *Talanta* **2009**, *79*, 103–108.

(21) Dahan, M.; Laurence, T.; Pinaud, F.; Chemla, D. S.; Alivisatos, A. P.; Sauer, M.; Weiss, S. Time-Gated Biological Imaging by Use of Colloidal Quantum Dots. *Opt. Lett.* **2001**, *26*, 825–827.

(22) Mandal, G.; Darragh, M.; Wang, Y. A.; Heyes, C. D. Cadmium-Free Quantum Dots as Time-Gated Bioimaging Probes in Highly-Autofluorescent Human Breast Cancer Cells. *Chem. Commun.* **2013**, *49*, 624–626.

(23) Bouccara, S.; Fragola, A.; Giovanelli, E.; Sitbon, G.; Lequeux, N.; Pons, T.; Loriette, V. Time-Gated Cell Imaging Using Long Lifetime Near-Infrared-Emitting Quantum Dots for Autofluorescence Rejection. *J. Biomed. Opt.* **2014**, *19*, 051208–051208.

(24) Hirano, S.; Suzuki, K. T. Exposure, Metabolism, and Toxicity of Rare Earths and Related Compounds. *Environ. Health. Persp.* **1996**, *104*, 85–95.

(25) Yong, K.-T.; Law, W.-C.; Hu, R.; Ye, L.; Liu, L.; Swihart, M. T.; Prasad, P. N. Nanotoxicity Assessment of Quantum Dots: from Cellular to Primate Studies. *Chem. Soc. Rev.* **2013**, *42*, 1236−1250.

(26) Gu, L.; Hall, D. J.; Qin, Z.; Anglin, E.; Joo, J.; Mooney, D. J.; Howell, S. B.; Sailor, M. J. In Vivo Time-Gated Fluorescence Imaging with Biodegradable Luminescent Porous Silicon Nanoparticles. *Nat. Commun.* **2013**, *4*, 2326.

(27) Joo, J.; Liu, X.; Kotamraju, V. R.; Ruoslahti, E.; Nam, Y.; Sailor, M. J. Gated Luminescence Imaging of Silicon Nanoparticles. *ACS Nano* **2015**, *9*, 6233−6241.

(28) Tu, C.-C.; Chen, K.-P.; Yang, T.-A.; Chou, M.-Y.; Lin, L. Y.; Li, Y.-K. Silicon Quantum Dot Nanoparticles with Antifouling Coatings for Immunostaining on Live Cancer Cells. *ACS Appl. Mater. Interfaces* **2016**, *8*, 13714−13723.

(29) Lauerhaas, J. M.; Sailor, M. J. Chemical Modification of the Photoluminescence Quenching of Porous Silicon. *Science* **1993**, *261*, 1567−1568.

(30) Stewart, M. P.; Buriak, J. M. Exciton-Mediated Hydrosilylation on Photoluminescent Nanocrystalline Silicon. *J. Am. Chem. Soc.* **2001**, *123*, 7821−7830.

(31) Awasthi, K.; Nakabayashi, T.; Ohta, N. Effects of Nanosecond Pulsed Electric Fields on the Intracellular Function of HeLa Cells as Revealed by NADH Autofluorescence Microscopy. *ACS Omega* **2016**, *1*, 396−406.

(32) Islam, M. S.; Honma, M.; Nakabayashi, T.; Kinjo, M.; Ohta, N. pH Dependence of the Fluorescence Lifetime of FAD in Solution and in Cells. *Int. J. Mol. Sci.* **2013**, *14*, 1952−1963.

(33) Björkelund, H.; Gedda, L.; Barta, P.; Malmqvist, M.; Andersson, K. Gefitinib Induces Epidermal Growth Factor Receptor Dimers Which Alters the Interaction Characteristics with ^{125}I-EGF. *PLoS One* **2011**, *6*, e24739.